The insecticidal spider toxin SFI1 is a knottin peptide that blocks the pore of insect voltage-gated sodium channels via a large β-hairpin loop

Niraj S Bende[1], Sławomir Dziemborowicz[2], Volker Herzig[1], Venkatraman Ramanujam[3], Geoffrey W. Brown[4], Frank Bosmans[5,6], Graham M Nicholson[2], Glenn F King[1*], and Mehdi Mobli[3*]

[1]Institute for Molecular Bioscience, The University of Queensland, St. Lucia, QLD 4072, Australia; [2]School of Medical & Molecular Biosciences, University of Technology Sydney, NSW 2007, Australia; [3]Centre for Advanced Imaging, The University of Queensland, St. Lucia, QLD 4072, Australia, [4]Queensland Department of Agriculture, Fisheries and Forestry, Brisbane 4001 QLD, Australia; [5]Department of Physiology & [6]Solomon H. Snyder Department of Neuroscience, Johns Hopkins University, School of Medicine, Baltimore, MD 21205 USA;

**Address correspondence to:*

Glenn F. King (glenn.king@imb.uq.edu.au) or Mehdi Mobli (m.mobli@uq.edu.au).

Running title: Structure and function of the spider toxin Sf1a

Keywords: voltage-gated sodium channel, spider toxin, pore blocker, heteronuclear NMR, disulfide-rich peptide

Abstract

Spider venoms contain a plethora of insecticidal peptides that act on neuronal ion channels and receptors. Due to their high specificity, potency, and stability these peptides have attracted much attention as potential environmentally-friendly insecticides. Although many insecticidal spider-venom peptides have been isolated, the molecular target, mode of action and structure of only a small minority have been explored. Sf1a, a 46-residue peptide isolated from the venom of the tube-web spider *Segesteria florentina*, is insecticidal to a wide range of insects but non-toxic to vertebrates. In order to investigate its structure and mode of action, we developed an efficient bacterial expression system for production of Sf1a. We determined a high-resolution solution structure of Sf1a using multidimensional 3D/4D NMR spectroscopy. This revealed that Sf1a is a knottin peptide with an unusually large β-hairpin loop that accounts for a third of the peptide length. This loop is delimited by a fourth disulfide bond that is not commonly found in knottin peptides. We showed, through mutagenesis, that this large loop is functionally critical for insecticidal activity. Sf1a was further shown to be a selective inhibitor of insect voltage-gated sodium channels, consistent with its 'depressant' paralytic phenotype in insects. However, in contrast to the majority of spider-derived sodium channel toxins that function as gating modifiers via interaction with one or more of the voltage-sensor domains, Sf1a appears to act as a pore blocker.

1. Introduction

Despite intensive control measures, herbivorous insects reduce world crop yields by 10–14% and damage as much as 30% of stored grain [1, 2]. Insects also vector a wide range of human diseases including malaria, dengue, and Chagas disease [3]. Half of the world's population is at risk of contracting insect-borne diseases[4], with malaria alone causing ~3000 deaths/day [5].

Chemical insecticides are the primary method of controlling insect pests [6]. Although there appears to be a vast array of extant chemical insecticides, there are in fact only a few major classes that act on a very small number of molecular targets in the insect nervous system [4, 7, 8]. These conditions have promoted the evolution of insecticide resistance, with more than 1000 arthropod species now resistant to one or more classes of chemical insecticide [9]. The evolution of insecticide resistance has led to the withdrawal of chemical insecticides that are no longer considered effective, while concerns about the adverse impact of certain classes of chemical insecticides on the environment and human health has also led to widespread de-registrations and use cancellations by regulatory authorities [8]. These developments, along with more stringent requirements for registration of new insecticides, have significantly reduced the number of available insecticides [8]. For example, over the period 2005–2009 the U.S. Environmental Protection Agency (EPA) de-registered or limited the use of 169 insecticides while only 9 new insecticides were registered [4]. Thus, we are being forced to combat an increasing insect-pest problem with a rapidly diminishing chemical arsenal, resulting in an urgent need to discover new and safe insecticidal compounds.

The success of transgenic plants expressing insecticidal Cry toxins from the bacterium *Bacillus*

thuringiensis has created a renewed interest in protein- and peptide-based insecticides [10]. Along with predatory beetles, spiders are the most successful insect predators on the planet and their venoms are replete with insecticidal peptide toxins [8, 11]. Remarkably, the venom of a single spider can contain as many as one thousand unique peptides [12, 13]. Although the EPA recently approved a spider-venom peptide for use as an insecticide (http://www.vestaron.com/epa-approval), very few insecticidal spider toxins have been sufficiently characterized to warrant consideration as bioinsecticides [8]. One promising candidate is SFI1 (U_2-segestritoxin-Sf1a, hereafter Sf1a), a 46-residue peptide isolated from the venom of the tube-web spider *Segestria florentina* [14]. When injected into tobacco budworms (larvae of the noctuid moth *Heliothis virescens*), Sf1a induced flaccid paralysis within 15 min and killed larvae within 24 h, with an LD_{50} of 10 μg/g (~2 nmol/g) [14]. Moreover, Sf1a did not induce toxic effects in mice when injected intravenously at a dose of 1.5 mg/kg (~300 pmol/g).

Since spiders inject venom into prey via hypodermic-needle-like fangs, there is no evolutionary selection pressure for spider toxins to be orally active. Although some insecticidal spider-venom peptides are orally active [15, 16] this is not the case for Sf1a [17]. However, the oral activity of Sf1a can be markedly improved by fusion to the plant lectin GNA (*Galanthus nivalis* agglutinin), which ferries attached peptide toxins across the gut epithelium via transcytosis and effectively delivers them to the hemocoel, Malpighian tubules, fat bodies, ovarioles, and central nervous system [18-20]. Using this approach, Sf1a was found to be highly insecticidal when fed to a range of insects, including the tomato moth *Lacanobia oleracea* [17], the peach-potato aphid *Myzus persicae* [21] and the rice brown planthopper *Nilaparvata lugens* [21].

The structure and mode of action of Sf1a remain unknown. Here, we describe the development of an efficient *E. coli* expression system for production of Sf1a for structural and functional studies. We show that recombinant Sf1a is insecticidal to sheep blowflies (*Lucilia cuprina*) and we demonstrate that it acts by inhibiting insect voltage-gated sodium (Na_V) channels and not voltage-gated calcium (Ca_V) channels as initially suggested based on sequence homology. Moreover, we demonstrate that Sf1a inhibits insect Na_V channels by blocking the pore of the channel and not by the more typical allosteric voltage-dependent mechanism reported for other spider toxins that act as gating-modifiers [14]. The three-dimensional (3D) solution structure of Sf1a that we determined using multidimensional heteronuclear NMR spectroscopy revealed that it contains an inhibitor cystine knot (ICK) motif that is commonly observed in spider-venom peptides [8, 22, 23]. However, Sf1a contains an unusually large and disordered β-hairpin loop that is stabilized by an atypical fourth disulfide bond that anchors the ends of the loop. We show that this large β-hairpin loop contains a conserved sequence motif that is critical for the toxin's insecticidal activity.

2. Results

2.1 Production of recombinant Sf1a

Recombinant production of venom peptide toxins is often challenging due to presence of multiple disulfide bonds, which cannot be formed in the cytoplasm of most prokaryotic and eukaryotic cells due to the reducing intracellular environment. An approach that has proved successful for expression of disulfide-rich spider toxins is production in the periplasm of *E. coli*, where the enzymes involved in disulfide-bond formation are located [24]. Thus, to produce Sf1a, we employed an isopropyl-β-D-thiogalactopyranoside (IPTG)-inducible construct (Fig. 1A) that

allowed export of a His_6-MBP-toxin fusion protein to the *E. coli* periplasm. Using this expression system, a significant amount of His_6-MBP-toxin fusion protein (>5 mg/litre) was recovered in the soluble cell fraction following IPTG induction. The native toxin was recovered after cleavage of the His_6-MBP-Sf1a fusion protein using tobacco etch virus (TEV) protease. The initial construct, however, yielded a very small amount of cleaved product due to the native N-terminal Lys residue, which is not one of the preferred residues for the P1' position of TEV protease [25]. To improve the yield of cleaved protein, a non-native Ser residue, one of the two most preferred P1' residues for TEV protease, was added to the N-terminus of Sf1a. This recombinant Sf1a (referred to hereafter as rSf1a) was found to be equipotent with the initial construct having the native sequence and adopted the same tertiary fold as assessed by 1D ^{1}H NMR. Thus, this construct was used in all subsequent experiments. However, the amino acid residue numbering used throughout this article is for the native sequence.

The His_6-MBP-rSf1a fusion protein was purified using nickel affinity chromatography (Fig 1C, lanes 1–4). There was minimal loss of fusion protein in the flow through from the Ni-NTA beads (Fig. 1C, lanes 5–6). The bound fusion protein was eluted from the column and cleaved with His_6-tagged TEV protease (Fig. 1C, lanes 7–8). The His_6-tagged MBP and TEV protease were then removed by passage through a solid-phase extraction (SPE) column (Fig. 1D), and rSf1a subsequently purified using reverse-phase (RP) HPLC. rSf1a eluted as a single major disulfide-bond isomer with a retention time of ~25 min under the chosen experimental conditions. The purity of rSf1a was assessed to be >98% as judged by SDS-PAGE and matrix-assisted laser-desorption ionization time-of-flight mass spectrometry (MALDI-TOF MS) (Fig. 1D, inset). The final yield of rSf1a was ~2 mg of toxin per litre of culture.

2.2 rSf1a is lethal to insects

Depending on the dose, rSf1a induced uncoordinated movements within 5–10 min following injection into sheep blowflies (*L. cuprina*) and full paralysis within 15–60 min. Flies remained paralysed until 24 h when final paralysis statistics were recorded. Despite being almost completely paralysed and unable to make whole-body movements, flies still showed minor movements of the proboscis or extremities, even when injected with the highest doses of Sf1a. Lethality at 24 h remained below 20%. The median paralytic dose (PD_{50}) values for native Sf1a and rSf1a were determined to be 2.2 ± 0.2 nmol/g and 1.5 ± 0.3 nmol/g, respectively, which were not significantly different (unpaired *t*-test, $n = 3$, $p > 0.05$).

2.3.1 rSf1a is a Na_V channel pore blocker

We first investigated whether rSf1a modulated the activity of insect Na_V channels. Whole-cell sodium currents (I_{Na}) were recorded from dorsal unpaired median (DUM) neurons isolated from the American cockroach *Periplaneta americana*. The voltage-clamp configuration was used and depolarizing test pulses to –10 mV from a holding potential (V_h) of –90 mV (Fig. 2Ba) were employed to elicit fast activating and inactivating inward I_{Na}. During a 5-min perfusion, 1 µM rSf1a caused rapid inhibition of peak I_{Na} amplitude (55.7 ± 6.2% block of control peak I_{Na}, $p < 0.05$, $n = 4$; Fig. 2A,E) that was only partially reversible (~25% recovery) after prolonged washout in toxin-free solution. Interestingly, even a very high rSf1a concentrations (10 µM) failed to completely block I_{Na} (60.0 ± 5.0% block of control peak I_{Na}, $p < 0.05$, $n = 3$; Fig. 2C) while 300 nM rSf1a failed to produce significant inhibition (7.0 ± 0.6% block of control peak I_{Na}, $p > 0.05$, $n = 11$; Fig. 2D). At both 1 and 10 µM, rSf1a failed to alter the kinetics of Na_V channel activation or inactivation (Fig. 2A,C). To test if a series of depolarizing pulses could cause

dissociation of the toxin, post-pulses to +140 mV were applied immediately following a test pulse to –10 mV from a V_h of –90 mV (Fig. 2Bb). However, the depolarizing post-pulses failed to cause any significant relief from the fractional block of I_{Na} by 1 µM rSf1a compared with currents recorded in the absence of rSf1a ($p > 0.05$, $n = 5$; Fig. 2F).

To investigate whether rSf1a-induced inhibition of peak I_{Na} was due to a depolarizing shift in the voltage dependence of Na_V channel activation, peak I_{Na} amplitude was tested as a function of membrane potential (I_{Na}-V). Families of I_{Na} were elicited using a test pulse (V_{test}) that depolarized the cell from a V_h of –90 mV to +70 mV for 50 ms in 10-mV increments (Fig. 3A) before (Fig. 3C), and after (Fig. 3D), application of 1 µM rSf1a. Peak I_{Na} were then normalized against the maximum peak I_{Na} in the control and plotted against membrane potential (V_m) to establish an I_{Na}-V curve. Peak I_{Na} were then fitted to Eq. 1 (see Section 2.8) using non-linear regression analysis (Fig. 3E). In the absence of toxin, I_{Na} activated at around –50 mV, which did not shift in the presence of rSf1a (Fig. 3E). The voltage at half maximum Na_V channel activation ($V_{0.5}$) in control cells was only marginally shifted (1.4 mV) in the depolarizing direction in the presence of 1 µM rSf1a (control: $V_{0.5} = –21.4 \pm 1.3$ mV; slope factor = 5.1 ± 1.0 versus toxin: $V_{0.5} = –20.0 \pm 1.1$ mV; slope factor = 5.4 ± 0.8; $n = 4$, $p > 0.05$; Fig. 3E). This is more clearly observed as a lack of any significant shift in the voltage dependence of activation when currents recorded in the presence of toxin were normalized to the peak inward I_{Na} in the presence of toxin (Fig. 3F). This also revealed that the inhibition of Na_V channels by 1 µM rSf1a was voltage-independent and the binding of the toxin to the channel was not relieved at increasing membrane potentials, supporting the finding of the experiments using depolarizing post-pulses.

The effects of rSf1a on the voltage dependence of steady-state Na_V channel inactivation (h_∞-V) was also examined to determine whether the reduction of peak I_{Na} was due to stabilization of the inactivated (closed) state of the channel, and hence a reduction in channel availability, as opposed to a pore blocking mechanism. Accordingly, experiments were conducted using a two-pulse protocol that utilized a 1-s conditioning prepulse ($V_{prepulse}$) from –120 mV to 0 mV in 10-mV increments, followed by a 50-ms test pulse (V_{test}) to –10 mV (Fig. 3B). In the presence of 1 µM rSf1a, I_{Na} were inhibited to 51 ± 2% (n = 3) of control peak amplitude (parameter 'A' in Eq. 2; Fig. 3G). Normalization of the toxin data to the maximum peak I_{Na} in the presence of toxin revealed that the curves almost completely overlap (Fig. 3H) with no significant shift in h_∞-V (control: $V_{0.5}$ = –33.8 ± 0.3 mV and toxin: $V_{0.5}$ = –35.5 ± 0.8 mV: $p > 0.05$, n = 3; Fig. 3H). Thus, the 49% reduction in I_{Na} does not appear to be the result of a reduction in Na_V channel availability due to stabilization of the channels in the closed-inactivated state. Thus, rSf1a appears to be a Na_V channel pore blocker.

2.3.2 rSf1a has no significant effect on Ca_V or K_V channels

Given that Na_V channel-targeting spider toxins may also interact with Ca_V channels [26], we tested the ability of rSf1a to modulate the activity of insect Ca_V channels. At least two subtypes of Ca_V channel currents have been demonstrated in cockroach DUM neurons, including high-voltage-activated (HVA) and mid/low-voltage-activated (M-LVA) Ca_V channel currents [27-30]. Unfortunately, despite differences in the kinetic and pharmacological properties of M-LVA and HVA Ca_V channel currents, there remains no mechanism for recording one current in isolation from the other as no peptide or organic blockers are available that exclusively block one type of current [27]. As previously described, depolarizing voltage command pulses to different levels

were used to investigate actions on M-LVA and HVA Ca_V channels, respectively [30-32]. Ca_V channel barium currents (I_{Ba}) were evoked by 50-ms depolarizing pulses from a V_h of –90 mV at 7-s intervals to –30 mV for generation of predominantly M-LVA Ca_V channel currents and to +20 mV to evoke mainly HVA Ca_V channel currents (Fig. 4Ca) [27, 30]. Depolarizations to –30 mV caused an inward I_{Ba} with slow inactivation, consistent with a reduction in Ca^{2+}-dependent fast inactivation due to the use of Ba^{2+} as the charge carrier [27], whereas depolarizations to +20 mV elicited a smaller I_{Ba} with a faster inactivating component (Fig. 4A,B). Following a 5-min perfusion, 1 μM rSf1a caused only weak inhibition of both M-LVA and HVA Ca_V channel currents. The M-LVA Ca_V channel currents were reduced by 31.5 ± 44.0.% ($p > 0.05$, $n = 5$) and HVA Ca_V channel currents by 11.5 ± 9.7% ($p > 0.05$, $n = 5$). There were also no significant changes in M-LVA and HVA I_{Ba} activation and inactivation kinetics (Fig. 4A,B).

To investigate whether there was any shift in the threshold of Ca_V channel activation, I_{Ba}-V relationships were established from families of I_{Ba} generated by 100-ms depolarizing test potentials from V_h of –90 mV to +40 mV, at 10-mV increments every 7 s (Fig. 4Cb). Families of peak inward I_{Ba} were normalized against the maximum control inward peak I_{Ba} and plotted against the membrane potential. In controls, DUM neuron Ca_V channels activated between –50 mV and –40 mV. In the presence of 1 μM rSf1a this threshold was shifted slightly in the hyperpolarizing direction (Fig. 4D). This may be the cause of the large variance in the magnitude of inhibition of M-LVA Ca_V channel currents, detailed above. However, there was no significant shift in the $V_{0.5}$ of channel activation (control: $V_{0.5} = –29 ± 1$ mV versus toxin: $V_{0.5} = –27 ± 1$ mV; $n = 5$, $p > 0.05$) and currents were essentially superimposable when the toxin data was normalized to the maximum peak I_{Ba} in the presence of toxin (dotted line, Fig. 4D).

For completeness, we also determined the effect of rSf1a on the major outward K_V channel current subtypes present in cockroach DUM neurons. These include a slowly activating delayed-rectifier [$I_{K(DR)}$], transient 'A-type' [$I_{K(A)}$], and large-conductance Ca^{2+}-activated [$I_{BK(Ca)}$] voltage-gated potassium (K_V) channel currents [33]. To determine the effects of 1 μM rSf1a on K_V channels, global K_V channel currents (I_K) were generated by 50-ms depolarizing test pulses to +30 mV from a V_h of –80 mV, every 5 s (Fig. 4Fa). Global I_K were measured at the peak (circles) and at the end of the test pulse (50 ms, squares). The early peak global I_K results mainly from the contribution of rapidly activating $I_{K(A)}$ and $I_{BK(Ca)}$, while the late global I_K results from the slowly activating $I_{K(DR)}$ and slow inactivating component of the $I_{BK(Ca)}$. Application of 1 μM rSf1a caused a non-significant inhibition of outward global I_K reducing the peak global I_K by 18 ± 15% and the late global I_K by 18 ± 13% ($p > 0.05$ in both cases, $n = 3$; Fig. 4E). This lack of overt activity was mirrored by the lack of effect on the voltage-dependence of global I_K activation. Global I_K-V relationships generated by the pulse protocol shown in Fig. 4Fb were not significantly altered, with no marked differences in $V_{0.5}$ values between the I_K-V for controls ($V_{0.5}$ = –5 ± 2 mV for early and –8 ± 4 mV for late I_K) versus toxin ($V_{0.5}$ = –7 ± 3 mV for early and –8 ± 4 mV for late I_K) ($p > 0.05$; $n = 3$; Fig. 4G-H). Currents were essentially superimposable when the toxin data was normalized to maximum peak global I_K in the presence of toxin (dotted lines, Figs. 4G-H).

2.4 High-resolution solution structure of rSf1a

Buffer conductivity and pH can have a pronounced effect on NMR spectra and thus several conditions were screened to optimize NMR data quality, including 20 mM phosphate buffer, pH 6; 20 mM MES buffer, pH 6; 20 mM acetate buffer, pH 5; 20 mM citrate buffer pH 4.0; and 20 mM citrate buffer, pH 3.5. These buffer screens revealed that the sidechain of Trp33 exists in

several stable conformations and that the population of the minor conformations was reduced at low pH and high temperature. Trp33 is adjacent to Pro32 and therefore *cis-trans* isomerization of the Arg31-Pro32 peptide bond might be responsible for the observed conformational isomerism [34]. Such conformational dynamics are known to be both temperature and pH dependent [35].

Consequently, NMR data were collected at 40˚C using $^{13}C/^{15}N$-labelled rSf1a dissolved in 20 mM citrate buffer, pH 3.5. $^{1}H_N$, ^{15}N, $^{13}C_\alpha$, $^{13}C_\beta$, and ^{13}C resonance assignments were obtained from analysis of amide-proton strips in 3D HNCACB, CBCA(CO)NH, and HNCO spectra. Sidechain ^{1}H and ^{13}C chemical shifts were obtained using a 4D HCC(CO)NH-TOCSY experiment, which has the advantage of providing sidechain ^{1}H-^{13}C connectivities [36]. A fully assigned ^{1}H-^{15}N HSQC spectrum of rSf1a is shown in Fig. 5. Complete chemical shift assignments have been deposited in BioMagResBank (Accession Number 19535).

CYANA was used for automated NOESY assignment and structure calculation [37]. Disulfide-bond connectivities were determined from ^{15}N and ^{13}C NOESY spectra and confirmed by performing structure calculations without inclusion of disulfide-bond restraints. The following connectivities were unambiguously established following this procedure: Cys3-Cys19, Cys10-Cys22, Cys18-Cys42, and Cys24-Cys40, which corresponds to a 1–4, 2–5, 3–8, 6–7 framework, as described previously for Aps III [8]. For structure calculations, interproton distance restraints were supplemented with 75 dihedral-angle restraints (36 ϕ, 39 ψ) derived from TALOS+ chemical shift analysis [38]. 200 structures were calculated from random starting conformations, then the 20 structures with the lowest target function values were selected to represent the solution structure of rSf1a. Coordinates for the final ensemble of structures have been deposited

in the Protein Data Bank (Accession Number 2MF3).

The final ensemble of structures revealed that Sf1a contains a canonical ICK motif [39] (Fig. 6A) in which the Cys10-Cys22 and Cys3-Cys19 disulfide bonds and the intervening section of the peptide backbone form a ring that is pierced by the Cys18-Cys42 disulfide bond (Fig. 6B). The Cys24-Cys40 disulfide acts as a "molecular staple" to hold together the ends of the extended β-hairpin loop. This loop was poorly defined in the calculated structures and analysis of random coil indices by TALOS+ clearly shows that this loop is disordered (S^2 ~0.65 compared to average of ~0.8 for the core of the molecule). When the disordered hairpin loop and N-terminal residues are excluded, the ensemble of 20 structures overlay very well, with backbone and heavy-atom RMSDs of 0.13 Å and 0.43 Å, respectively, over residues 4–26 and 39–45. Based on precision and Ramachandran plot quality (see Table 1), the structure ranks as high resolution [40]. The structure has high stereochemical quality with a mean MolProbity [41] score of 1.55 ± 0.18, placing it in the 93rd percentile relative to other protein structures.

A search for structural homologs [42] revealed that rSf1a has similar topology to numerous other spider toxins containing the ICK motif. However, this search also revealed close structural homology to tachystatin B (PDB 2DCV), an antimicrobial ICK-containing peptide isolated from the Japanese horseshoe crab *Tachypleus tridentatus* [43]. Tachystatin B does not contain the extended hairpin loop found in rSf1a but the two peptides overlay well over their core ICK regions (Fig. 6C). A similarly large hairpin loop is present in the structure of the insecticidal spider-venom peptide Aps III (μ-CUTX-As1a) [8]. In Aps III this loop is comprised of 14 residues, which is larger than found in typical ICK peptides but significantly shorter than the 19-

residue loop present in rSf1a. An overlay of the structures of rSf1a and Aps III reveals that the placement of the non-ICK disulfide bond is very different in the two peptides (Fig. 6C).

2.5 Functional importance of the β-hairpin loop

The β-hairpin loop in spider-venom ICK peptides often houses functionally critical residues [7]. The unusually large β-hairpin loop found in Sf1a contains an Arg-Pro-Trp (RPW) motif that is strictly conserved in this family of toxins [14] and we therefore wondered whether this motif might be critical for the toxin's insecticidal activity.

We produced a mutant of rSf1a in which residues R31 and W33 were both replaced with alanine. The mutant peptide (rSf1a-R31A/W33A) was purified and characterized as described above for rSf1a and shown to adopt the same fold as the native peptide by comparison of their 2D ^{1}H-^{15}N HSQC spectra. In striking contrast to rSf1a (PD_{50} = 1.5 nmol/g), the R31A/W33A double mutant was not insecticidal to blowflies at doses up to 95.4 nmol/g (i.e. there were no signs of paralysis or lethality up to 24 h after injection). Moreover, at a concentration of 1 μM, the rSf1a-R31A/W33A mutant failed to significantly inhibit I_{Na} in DUM neurons (5.9 ± 1.8% block of control peak I_{Na}, $p > 0.05$, $n = 3$; Fig. 2D), consistent with its lack of insecticidal activity. We therefore conclude that the β-hairpin loop, and in particular the conserved RPW motif, is critical for the activity of Sf1a.

3. Discussion

3.1 Molecular target of Sf1a

We examined the effect of rSf1a on insect Na_V, Ca_V and K_V channels that represent common

targets for insecticidal spider toxins. The main effect of rSf1a was to produce a rapid, but incomplete, block of insect Na_V channels that occurred in the absence of: (i) a shift in the voltage dependence of activation; (ii) a shift in the voltage dependence of steady-state inactivation; or (iii) depolarization-induced dissociation of binding. Furthermore, Sf1a failed to modulate the gating or kinetics of Na_V channel currents and the inhibition of I_{Na} was not relieved by depolarizing pulses. We also showed that rSf1a does not significantly affect the activity of insect Ca_V channels nor delayed-rectifier, 'A-type' or B_{KCa} potassium channels that are the major contributors to the global outward Kv channel current in cockroach DUM neurons. Thus, rSf1a appears to be a channel blocker that selectively plugs the outer vestibule of Na_V channels in a manner similar to μ-conotoxins [45]. The incomplete block of Na^+ flux induced by rSf1a is consistent with the toxin binding to the channel outer vestibule rather then lodging deep into the pore region and causing complete steric block of the insect Na_V channel pore. [44].

Most other Na_V channel blockers isolated from spider venoms act as 'gating-modifiers' that reduce I_{Na} by causing a depolarizing shift in the voltage-dependence of Na_V channel activation, thereby inducing a flaccid or 'depressant' phenotype. This results from an interaction with one, or more, of the four Na_V channel voltage sensors [46]. These spider toxins include the depressant theraphotoxins β-TRTX-Cm1a, -Cm1b and Cm2a (ceratotoxin-1, -2 and -3) from *Ceratogyrus marshalli* and β-theraphotoxin-Ps1a from *Paraphysa scrofa* [47]. In contrast, rSf1a inhibits insect Na_V channel conductance in the absence of any depolarizing shift in the voltage-dependence of activation. Given this distinct lack of any voltage-dependent shift in channel activation, Sf1a belongs to a growing group of spider μ-toxins that appear to occlude the outer vestibule of the insect Na_V channel. This includes Aps III (μ-CUTX-As1a) from the unrelated spider *Apomastus*

schlingeri [8]. Unlike Aps III, which acts on both Na_v and to a lesser extent Ca_v channels, rSf1a selectively blocks insect Na_v channels. Furthermore, Sf1a is marginally more potent than two other μ-theraphotoxins that are pore-blockers: μ-TRTX-Hhn2b (hainantoxin-I) and μ-TRTX-Hh1a (huwentoxin-III) from two different species of Chinese *Haplopelma* tarantulas. These two toxins block insect Na_V channels presumably via binding to neurotoxin receptor site-1 near the mouth of the channel with IC_{50} concentrations for block of the channel between 1.1 and 4.5 μM [48, 49]. While the IC_{50} for Sf1a on insect Na_V channels was not definitively determined in the present study, it is <1 μM as this concentration caused a 60% block of cockroach DUM neuron I_{Na}. Thus, although both μ-TRTX-Hhn2b and μ-TRTX-Hh1a selectively inhibit insect Na_V channels, rSf1a targets the insect Na_V channel with higher affinity, consistent with its modest, but irreversible, depressant paralytic activity (PD_{50} = 1.5 nmol/g).

An additional mechanism that can lead to an inhibition of I_{Na} is a decrease in Na_V channel availability, as observed with μ-TMTX-Hme1a from venom of the spider *Heriaeus melloteei* [50]. This mechanism of action causes an increase in the number of Na_V channels stabilized in the closed-inactivated state as observed by a hyperpolarizing shift in the voltage-dependence of steady-state inactivation. In contrast to μ-TMTX-Hme1a, rSf1a failed to produce any significant hyperpolarizing shift in the voltage-dependence of steady-state Na_V channel inactivation lending further support to the notion that the toxin occludes the outer vestibule of the channel.

Finally, voltage-dependent dissociation of bound toxins from mammalian and insect Na_V channels has also previously been demonstrated with a range of spider, scorpion and sea anemone toxins [51-55]. However, there was no indication of voltage-dependent dissociation of rSf1a from

DUM neurons using depolarizing post-pulse protocols.

In summary, rSf1a inhibits Na_V channels via partial block of the channel pore. This inhibition occurs in the absence of any alteration to the kinetics of Na_V channel inactivation as observed for spider δ-toxins [56] and Sf1a fails to produce any hyperpolarizing shift (as seen for excitatory β-toxins [57]) or a depolarizing shift (as observed for depressant β-toxins [58]) in the voltage-dependence of Na_V channel activation. Based on the pharmacology described here, rSf1a should be renamed μ-segestritoxin-Sf1a (μ-SGTX-Sf1a) based on the rational nomenclature recently proposed for spider-venom peptides [59]. This is consistent with its action to induce flaccid paralysis, in contrast with the spastic paralysis observed with spider δ-toxins [60] and excitatory β-toxins [61].

The incomplete block of Na_V channels is unlikely to be the sole cause of Sf1a toxicity. Given the weak effects of Sf1a on neuronal calcium channels, an additional target might be the HVA-like dihydropyridine-sensitive Ca_V channels found on the surface of invertebrate skeletal muscle [28], which are critical for conduction of muscle action potentials.

3.2 Unusual structure of Sf1a

The ICK/knottin topology is by far the dominant structural scaffold found in spider venoms [8] and it is therefore not surprising to find that rSf1a conforms to this paradigm. Many spider-venom knottins are elaborated with a fourth non-ICK disulfide bond such as the δ-hexatoxins with 1–4, 2-6, 3–7, 5–8 connectivity [62] and the κ-hexatoxins that contain a rare vicinal disulfide bond leading to 1–6, 2–7, 3–4, 5–8 connectivity [63, 64]. However, the 1–4, 2–5, 6–7,

3–8 disulfide connectivity seen in rSf1a is rare and has only been described for the following spider toxins: Aps III (PDB 2M36) [8], U_2-hexatoxin-Hi1a (PDB 1KQH/1KQI) [34], ω-agatoxin IVA (PDB 1IVA) [65], δ-palutoxin IT2 (PDB 1V91) [66] and μ-agatoxin I (PDB 1EIT) [67]. In all these structures except for Aps III, the non-ICK disulfide bond delineates the boundaries of a 4–6 residue loop, potentially as a mechanism for decoupling the dynamics of the loop from the ICK core. In Aps III the auxiliary disulfide bond appears to stabilise a dynamic glycine-rich segment within the loop [8]. Notably, in rSf1a this loop comprises 19 residues, making up a third of the entire peptide sequence, making it by far the largest such loop described for any ICK peptide in this class. C*is-trans* isomerization of the Tyr29-Pro30 peptide bond in the loop region of U_2-hexatoxin-Hi1a leads to an equilibrium between two equally populated conformers. In rSf1a, we observed multiple conformations of the tryptophan residue adjacent to Pro32, but the minor conformers made up a small fraction of the equilibrium population.

The unusual β-hairpin loop in rSf1a was found to be functionally critical. Simultaneous mutation of R31 and W33 within the conserved RPW motif in the β-hairpin loop led to a mutant toxin that lacked insecticidal activity and was able to inhibit insect Na_V channel currents. The only other peptide in this class of knottins for which the pharmacophore has been mapped is δ-palutoxin IT2 and in this case the β-hairpin loop was also found to be functionally important [66].

Finally, we note that the second closest structural homolog of rSf1a is tachystatin B, an antimicrobial peptide isolated from the Japanese horseshoe crab *Tachypleus tridentatus* [43]. The two peptides overlay very closely over their core ICK regions, but deviate significantly over the unusually large disordered loop of rSf1a. The origin of the ICK fold remains under debate; there

is conflicting evidence about whether the ICK motif evolved from an ancestral two-disulfide, disulfide-directed β-hairpin (DDH) fold by addition of a disulfide bond [63, 69] or vice versa [70]. The presence of the ICK fold in an ancient marine arthropod suggests that the ICK fold may have already been present prior to its recruitment into the venom of arthropods. In this scenario, the ICK fold would be the plesiotypic state with the DDH fold subsequently evolving via loss of a disulfide bond. This would provide an alternative explanation for the rarity of DDH peptides in arachnid venoms [69].

3.3 Sf1a as a bioinsecticide

We found that Sf1a caused a long-lasting, irreversible paralysis in sheep blowflies that eventually led to death by starvation. Due to methodological issues (i.e. high mortality in controls beyond 24 h), we could not determine the PD_{50} at longer time periods. However, flies paralysed by high doses of rSf1a remained paralysed 48 h after injection The observed effects of rSf1a in blowflies are similar to those recently reported for the spider-venom peptide Aps III, although Aps III is 3-fold more potent with a PD_{50} of 700 pmol/g [8]. Given the observed insecticidal effects of rSf1a in blowflies, it seems likely that it would produce similar effects in dipteran pests such as mosquitoes and tsetse flies that vector human diseases. Since rSf1a is also active against lepidopteran [14, 17] and hemipteran [21] pests, but inactive against vertebrates [14], it appears to be a suitable lead for development of novel bioinsecticides [4]. Although the moderate potency of Sf1a would require large amounts to be applied in the field for efficient pest control, delivery of the toxin to pest insects via genetic engineering of crops or via insect-specific pathogens (e.g., entomopathogenic fungi) might provide efficient delivery of the toxin at effective concentrations.

In summary, we have shown that Sf1a is a Na_V channel-specific insecticidal toxin that acts via a non-voltage dependent mechanism. This is an atypical mode of action that has previously only been observed in one other spider toxin, namely Aps III. Although less potent than Aps III, the specificity of Sf1a towards Na_V channels makes it an attractive pharmacological tool.

4. Material and Methods

4.1. Chemicals

All chemicals were purchased from Sigma-Aldrich Australia (Castle Hill, NSW, Australia), Sigma-Aldrich USA (St Louis, MO, USA), or Merck Chemicals (Kilsyth, Victoria, Australia) with the exception of IPTG (Life Technologies, Victoria, Australia) and HPLC-grade acetonitrile (RCI Labscan, Bangkok, Thailand). $^{13}C_6$-glucose and $^{15}NH_4Cl$ were purchased from Sigma-Aldrich Australia. Recombinant His_6-TEV protease (EC 3.4.22.44) was produced in-house using a previously described protocol [71].

4.2 Nomenclature

Based on the rational nomenclature proposed for spider-venom peptides [59], SFI1 should be renamed μ-segestritoxin-Sf1a (μ-SGTX-Sf1a) based on its source and activity on Na_V channels.

4.3 Production of recombinant Sf1a

A synthetic gene encoding Sf1a, with codons optimized for expression in *E. coli*, was synthesized and cloned into the pLIC-MBP expression vector by GeneArt (Invitrogen, Regensburg, Germany). This vector (pLIC-NSB2), which was designed as described earlier [8], encodes an IPTG-inducible LacI promoter, a MalE signal sequence for periplasmic export, a His_6 tag for nickel affinity purification, maltose-binding protein (MBP) fusion tag to enhance solubility, and a TEV protease cleavage site between the MBP and Sf1a coding regions (Fig. 1A). The plasmid was transformed into *E. coli* strain BL21(λDE3) for rSf1a production. Cultures were grown in Terrific Broth (TB) medium using baffled flasks at 37°C with shaking at 110 rpm. Expression of the toxin gene was induced with 1 mM IPTG at an OD_{600} of 0.9–1.0, then cells were grown at

18°C for a further 15 h and harvested by centrifugation for 12 min at 6000 rpm. For production of uniformly $^{13}C/^{15}N$-labelled Sf1a, cultures were grown in minimal medium supplemented with $^{13}C_6$-glucose and $^{15}NH_4Cl$ as the sole carbon and nitrogen sources, respectively.

The His_6-MBP-rSf1a fusion protein was extracted from the bacterial periplasm by cell disruption at 27 kPa (TS Series Cell Disrupter, Constant Systems Ltd, Northants, UK), then captured by passing the periplasmic extract (buffered in 40 mM Tris, 450 mM NaCl, pH 8.0) over Ni-NTA Superflow resin (Qiagen) followed by washing with 10 mM imidazole to remove any products that bound non-specifically to the resin. The fusion protein was then eluted with 500 mM imidazole. The eluted fusion protein was concentrated to 5 ml and then the buffer was exchanged to remove imidazole. Reduced and oxidized glutathione were then added to 0.6 mM and 0.4 mM, respectively, to maintain TEV protease activity. Approximately 100 μg of His_6-tagged TEV protease was added per mg of fusion protein, and then the cleavage reaction was allowed to proceed at room temperature for 12 h. The cleaved His_6-MBP and His_6-TEV were removed by using SPE columns; the mixtures was loaded onto the column and the peptide eluted with 40% elution solvent (Solvent B: 0.043% trifluoroacetic acid (TFA) in 90% acetonitrile). The eluate was lyophilized and then semi-pure rSf1a was subjected to further purification using RP-HPLC. RP-HPLC was performed on a Vydac C18 column (250 x 4.6 mm, particle size 5 μm) using a flow rate of 1 ml/min and a gradient of 20–40% Solvent B in Solvent A (0.05% TFA in water) over 20 min.

4.4 MALDI-TOF mass spectrometry

Peptide masses were determined using MALDI-TOF MS employing a Model 4700 Proteomics

Bioanalyser (Applied Biosystems, CA, USA). RP-HPLC fractions were mixed 1:1 (v:v) with α-cyano-4 hydroxycinnamic acid matrix (5 mg/ml in 50/50 acetonitrile/H_2O) and MALDI-TOF spectra were acquired in positive reflector mode. All reported masses are for monoisotopic $[M+H]^+$ ions.

4.5 Blowfly toxicity assay

Insect toxicity assays were performed as described previously [8] Briefly, rSf1a, nat-Sf1a or rSf1a-R31A/W33A were injected into the ventro-lateral thoracic region of sheep blowflies (*Lucilia cuprina*) weighing 19.5–25.9 mg. Three separate experiments were conducted for each Sf1a homolog, each comprising 3–10 doses, with each dose injected into ten flies. Paralytic and lethal effects were measured 24 h post-injection. PD_{50} values were calculated as described previously [8] with statistical analysis and unpaired Student's *t*-tests performed using Prism 6.

4.6 Structure determination

NMR spectra were acquired at 40°C on a 900 MHz NMR spectrometer (Bruker BioSpin, Germany) equipped with a cryogenically cooled probe. $^{15}N/^{13}C$-labelled rSf1a was dissolved in 20 mM citrate, pH 3.5 at a final peptide concentration of 420 μM, followed by addition of□5□□D_2O. The sample was filtered using a low-protein-binding Ultrafree-MC centrifugal filter (0.22 μm pore size; Millipore, MA, USA), then 300 μL was added to a susceptibility matched 5 mm outer-diameter microtube (Shigemi Inc., Japan).

3D and 4D spectra used for resonance assignments were acquired using non-uniform sampling (NUS) [72]. Sampling schedules that approximated the signal decay in each indirect dimension

were generated using sched3D [36]. NUS data were processed using the Rowland NMR toolkit (www.rowland.org/rnmrtk/toolkit.html) and maximum entropy parameters were automatically selected as previously described [73]. ^{13}C- and ^{15}N-edited HSQC-NOESY spectra (mixing time of 200 ms) were acquired using uniform sampling. Separate ^{13}C-edit HSQC-NOESY spectra were acquired for the aliphatic and aromatic regions of the carbon spectrum.

Dihedral angles were derived from TALOS+ chemical shift analysis [38] and the restraint range for structure calculations was set to twice the estimated standard deviation. NOESY spectra were manually peak picked and integrated, peak lists were then automatically assigned, distance restraints extracted, and an ensemble of structures calculated using the torsion angle dynamics package CYANA 3.0 [37]. The tolerances used for CYANA were 0.02 ppm in the direct ^{1}H dimension, 0.04 ppm in the indirect ^{1}H dimension, and 0.4 ppm for the heteronucleus (^{13}C/^{15}N). During the automated NOESY assignment/structure calculation process, CYANA assigned 92% of all NOESY crosspeaks (1447 out of 1566). The four disulfide bonds were assigned based on preliminary structure calculations; subsequent calculations included distance restraints for these disulfide bonds as described previously [74].

4.7 Electrophysiological measurements on insect neurons

DUM neurons were isolated from unsexed adult American cockroaches (*Periplaneta americana*) as described previously [8]. Briefly, terminal abdominal ganglia were removed and placed in normal insect saline (NIS) containing (in mM): NaCl 180, KCl 3.1, N-hydroxyethylpiperazine-N-ethanesulfonic acid (HEPES) 10 and D-glucose 20. Ganglia were then incubated in 1 mg/ml collagenase (type IA) for 40 min at 29°C. Following enzymatic treatment, ganglia were washed

twice in NIS and resuspended in NIS supplemented with 4 mM $MgCl_2$, 5 mM $CaCl_2$, 5% foetal bovine serum and 1% penicillin/streptomycin (Life Technologies, Victoria, Australia) (NIS+) and triturated through a fire-polished Pasteur pipette. The resultant cell suspension was then distributed onto 12-mm diameter glass coverslips pre-coated with 2 mg/ml concanavalin A (type IV). DUM neurons were maintained in NIS+ at 29°C and 100 % humidity. Ionic currents were recorded in voltage-clamp mode using the whole-cell patch-clamp technique, employing version 10.2 of the pCLAMP data acquisition system (Molecular Devices, Sunnyvale, CA). Data were filtered at 5–10 kHz with a low-pass Bessel filter with leakage and capacitive currents subtracted using *P*–*P*/4 procedures. Digital sampling rates were set between 15 and 25 kHz depending on the length of the protocol. Single-use 0.8–2.5 MΩ electrodes were pulled from borosilicate glass and fire-polished prior to current recordings. Liquid junction potentials were calculated using JPCALC [75], and all data were compensated for these values. Cells were bathed in external solution through a continuous pressurized perfusion system at 1 ml/min, while toxin solutions were introduced via direct pressurized application using a perfusion needle at ~50 µl/min (Automate Scientific, San Francisco, CA). Control data were not acquired until at least 20 min after whole-cell configuration was achieved to eliminate the influence of fast time-dependent shifts in steady-state inactivation resulting in rundown of I_{Na} from Na_V channels. All experiments were performed at ambient room temperature (20–23°C). To record I_{Na}, the external bath solution contained (in mM): NaCl 230, CsCl 5, $CaCl_2$ 1.8, tetraethylammonium chloride (TEA-Cl) 50, 4-aminopyridine (4-AP) 5, HEPES 10, $NiCl_2$ 0.1, and $CdCl_2$ 1, adjusted to pH 7.4 with 1 M NaOH. The pipette solution contained (in mM): NaCl 34, CsF 135, $MgCl_2$ 1, HEPES 10, ethylene glycol-bis(2-aminoethylether)-N,N,N′,N′-tetraacetic acid (EGTA) 5, and ATP-Na_2 3, adjusted to pH 7.4 with 1 M CsOH. To eliminate any influence of differences in osmotic pressure, all internal

and external solutions were adjusted to 400 ± 5 mOsmol/l with sucrose. Due to the reported current rundown with calcium as a charge carrier [27], $BaCl_2$ replaced $CaCl_2$ in all experiments on voltage-gated Ca_V channels. The external bath solution for I_{Ba} recordings contained (in mM): Na acetate 140, TEA-Br 30, $BaCl_2$ 3 and HEPES 10, adjusted to pH 7.4 with 1 M TEA-OH. The external solution also contained 300 nM tetrodotoxin (TTX) to block Na_V channels. Pipette solutions contained (in mM): Na acetate 10, CsCl 110, TEA-Br 50, ATP-Na_2 2, $CaCl_2$ 0.5, EGTA 10 and HEPES 10, adjusted to pH 7.4 with 1 M CsOH. The external bath solution for recording global K_V channel currents (I_K) contained (in mM): NaCl 200, K gluconate 50, $CaCl_2$ 5, $MgCl_2$ 4, TTX 0.3, HEPES 10 and D-glucose 10, adjusted to pH 7.4 with 1 M NaOH. The pipette solution consisted of (in mM): K gluconate 135, KF 25, NaCl 9, $CaCl_2$ 0.1, $MgCl_2$ 1, EGTA 1, HEPES 10 and ATP-Na_2 3, adjusted to pH 7.4 with 1 M KOH.

Experiments were rejected if there were large leak currents or currents showed signs of poor space clamping.

4.8 Curve fitting and statistical analysis

Peak current amplitude was analysed offline using AxoGraph X v1.5.3 (Molecular Devices). Current amplitudes were normalized against maximal control current amplitude, or maximal current amplitude in the presence of 1 µM rSf1a, for all curve-fitted data. All curve-fitting was performed using PRISM 6 for Windows (GraphPad Software Inc., San Diego, CA) using nonlinear regression and a least-squares method. Comparisons of two sample means were made using a paired Student's *t*-test. A test was considered to be significant when $p < 0.05$. All data represent the mean ± SEM of *n* independent experiments.

The data for the voltage dependence of channel activation, for all channel types, were fitted using the following current-voltage (*I-V*) formula:

$$I = g_{max}\left(1 - \left(\frac{1}{1+\exp[(V-V_{0.5})/s]}\right)\right)(V - V_{rev}) \qquad \text{Eq. 1}$$

where I is the amplitude of the current at a given test potential V, g_{max} is the maximal conductance, $V_{0.5}$ is the voltage at half-maximal activation, s is the slope factor and V_{rev} is the apparent reversal potential.

The data for voltage dependence of Na_V channel steady-state inactivation (h_∞/V) were amplitude inverted and fitted using the following Boltzmann equation:

$$h_\infty = \frac{A}{1+\exp\,[(V-V_{0.5})/k]} \qquad \text{Eq. 2}$$

where A is the fraction of control maximal peak I_{Na}, $V_{0.5}$ is the midpoint of inactivation, k is the slope factor, and V is the conditioning prepulse potential.

On-rates were determined by fitting timecourse data with the following single exponential association function:

$$Y = Y_0 + (A - Y_0) \times (1 - \exp(-K \times t)) \qquad \text{Eq. 3}$$

where Y_0 is the maximal peak I_{Na}, A is the minimum peak I_{Na}, K is the rate constant and t is time. The on-rate (τ_{on}) was subsequently determined from the inverse of the rate constant (K).

Acknowledgements

We thank the Queensland NMR Network for access to the 900 MHz NMR spectrometer at The University of Queensland. This work was supported by the Australian Research Council through Discovery Grants DP140101098 to MM and DP130103813 to GFK and a Future Fellowship to MM (FTl10100925). GFK is supported by a Principal Research Fellowship from the Australian National Health & Medical Research Council. NSB received support from University of Queensland International Research Tuition Award (UQIRTA) and University of Queensland Research Scholarship (UQRS).

Author contributions

Conceived and designed the experiments: NSB, SD, VH, FB, GMN, GFK, MM. Performed the experiments: NSB, SD, VH, VR, MM. Analyzed the data: NSB, SD, VH, GMN, MM. Contributed materials, experimental/analysis tools: NSB, SD, VH, GWB, GMN, GFK, MM. Wrote the paper: NSB, SD, VH, FB, GMN, GFK, MM.

References

1. Oerke EC (2006) Crop losses to pests, *J Agric Sci.* **144**, 31–43.
2. Boyer S, Zhang H & Lemperiere G (2012) A review of control methods and resistance mechanisms in stored-product insects, *Bull Entomol Res.* **102**, 213–229.
3. Tedford HW, Sollod BL, Maggio F & King GF (2004) Australian funnel-web spiders: master insecticide chemists, *Toxicon.* **43**, 601–618.
4. Windley MJ, Herzig V, Dziemborowicz SA, Hardy MC, King GF & Nicholson GM (2012) Spider-venom peptides as bioinsecticides, *Toxins.* **4**, 191–227.
5. Murray CJ, Rosenfeld LC, Lim SS, Andrews KG, Foreman KJ, Haring D, Fullman N, Naghavi M, Lozano R & Lopez AD (2012) Global malaria mortality between 1980 and 2010: a systematic analysis, *Lancet.* **379**, 413–431.
6. Smith JJ, Herzig V, King GF & Alewood PF (2013) The insecticidal potential of venom peptides, *Cell Mol Life Sci* **70**, 3665–3693.
7. Tedford HW, Gilles N, Menez A, Doering CJ, Zamponi GW & King GF (2004) Scanning mutagenesis of ω-atracotoxin-Hv1a reveals a spatially restricted epitope that confers selective activity against insect calcium channels, *J Biol Chem.* **279**, 44133–44140.
8. Bende NS, Kang E, Herzig V, Bosmans F, Nicholson GM, Mobli M & King GF (2013) The insecticidal neurotoxin Aps III is an atypical knottin peptide that potently blocks insect voltage-gated sodium channels, *Biochem Pharmacol.* **85**, 1542–1554.
9. Arthropod pesticide resistance database (2013) in http://www.pesticideresistance.org/.
10. Tabashnik BE, Brevault T & Carriere Y (2013) Insect resistance to *Bt* crops: lessons from the first billion acres, *Nat Biotechnol.* **31**, 510–521.
11. Michiels K, Van Damme EJ & Smagghe G (2010) Plant-insect interactions: what can we learn from plant lectins?, *Arch Insect Biochem Physiol.* **73**, 193–212.
12. Escoubas P, Sollod B & King GF (2006) Venom landscapes: mining the complexity of spider venoms via a combined cDNA and mass spectrometric approach, *Toxicon.* **47**, 650–663.
13. Palagi A, Koh JM, Leblanc M, Wilson D, Dutertre S, King GF, Nicholson GM & Escoubas P (2013) Unravelling the complex venom landscapes of lethal Australian funnel-web spiders (Hexathelidae: Atracinae) using LC-MALDI-TOF mass spectrometry, *J Proteomics.* **80**, 292–310.

14. Lipkin A, Kozlov S, Nosyreva E, Blake A, Windass JD & Grishin E (2002) Novel insecticidal toxins from the venom of the spider *Segestria florentina*, *Toxicon.* **40**, 125–130.
15. Mukherjee AK, Sollod BL, Wikel SK & King GF (2006) Orally active acaricidal peptide toxins from spider venom, *Toxicon.* **47**, 182–187.
16. Hardy MC, Daly NL, Mobli M, Morales RA & King GF (2013) Isolation of an orally active insecticidal toxin from the venom of an Australian tarantula, *PLoS One.* **8**, e73136.
17. Fitches E, Edwards MG, Mee C, Grishin E, Gatehouse AM, Edwards JP & Gatehouse JA (2004) Fusion proteins containing insect-specific toxins as pest control agents: snowdrop lectin delivers fused insecticidal spider venom toxin to insect haemolymph following oral ingestion, *J Insect Physiol.* **50**, 61–71.
18. Fitches E, Woodhouse SD, Edwards JP & Gatehouse JA (2001) *In vitro* and *in vivo* binding of snowdrop (*Galanthus nivalis* agglutinin; GNA) and jackbean (*Canavalia ensiformis*; Con A) lectins within tomato moth (*Lacanobia oleracea*) larvae; mechanisms of insecticidal action, *J Insect Physiol.* **47**, 777–787.
19. Fitches EC, Pyati P, King GF & Gatehouse JA (2012) Fusion to snowdrop lectin magnifies the oral activity of insecticidal ω-hexatoxin-Hv1a peptide by enabling its delivery to the central nervous system, *PLoS ONE.* **7**, e39389.
20. Bonning BC & Chougule NP (2014) Delivery of intrahemocoelic peptides for insect pest management, *Trends Biotech.* **32**, 91–98.
21. Down RE, Fitches EC, Wiles DP, Corti P, Bell HA, Gatehouse JA & Edwards JP (2006) Insecticidal spider venom toxin fused to snowdrop lectin is toxic to the peach-potato aphid, *Myzus persicae* (Hemiptera: Aphididae) and the rice brown planthopper, *Nilaparvata lugens* (Hemiptera: Delphacidae), *Pest Manag Sci.* **62**, 77–85.
22. King GF, Tedford HW & Maggio F (2002) Structure and function of insecticidal neurotoxins from Australian funnel-web spiders, *J Toxicol-Toxin Rev.* **21**, 359–389.
23. Saez NJ, Senff S, Jensen JE, Er SY, Herzig V, Rash LD & King GF (2010) Spider-venom peptides as therapeutics, *Toxins.* **2**, 2851–2871.
24. Klint JK, Senff S, Saez NJ, Seshadri R, Lau HY, Bende NS, Undheim EAB, Rash LD, Mobli M & King GF (2013) Production of recombinant disulfide-rich venom peptides for structural and functional analysis via expression in the periplasm of *E. coli*, *PLoS ONE.* **8**, e63865.

25. Kapust RB, Tozser J, Copeland TD & Waugh DS (2002) The P1' specificity of tobacco etch virus protease, *Biochem Biophys Rese Commun.* **294**, 949–955.
26. Klint JK, Senff S, Rupasinghe DB, Er SY, Herzig V, Nicholson GM & King GF (2012) Spider-venom peptides that target voltage-gated sodium channels: pharmacological tools and potential therapeutic leads, *Toxicon.* **60**, 478–491.
27. Wicher D & Penzlin H (1997) $Ca2^{+}$ currents in central insect neurons: electrophysiological and pharmacological properties, *J Neurophysiol.* **77**, 186–99.
28. Wicher D, Walther C & Wicher C (2001) Non-synaptic ion channels in insects—basic properties of currents and their modulation in neurons and skeletal muscles., *Prog Neurobiol.* **64**, 431–525.
29. Grolleau F & Lapied B (1996) Two distinct low-voltage-activated Ca^{2+} currents contribute to the pacemaker mechanism in cockroach dorsal unpaired median neurons, *J Neurophysiol.* **76**, 963–976.
30. Chong Y, Hayes JL, Sollod B, Wen S, Wilson DT, Hains PG, Hodgson WC, Broady KW, King GF & Nicholson GM (2007) The ω-atracotoxins: selective blockers of insect M-LVA and HVA calcium channels, *Biochem Pharmacol.* **74**, 623–638.
31. Wicher D & Penzlin H (1997) Ca^{2+} currents in central insect neurons: electrophysiological and pharmacological properties, *J Neurophysiol.* **77**, 186–199.
32. Wicher D, Walther C & Penzlin H (1994) Neurohormone D induces ionic current changes in cockroach central neurones, *J Comp Physiol A.* **174**, 507–515.
33. Windley MJ, Escoubas P, Valenzuela SM & Nicholson GM (2011) A novel family of insect-selective peptide neurotoxins targeting insect large-conductance calcium-activated K^{+} channels isolated from the venom of the theraphosid spider *Eucratoscelus constrictus*, *Mol Pharmacol.* **80**, 1–13.
34. Rosengren KJ, Wilson D, Daly NL, Alewood PF & Craik DJ (2002) Solution structures of the *cis*- and *trans*-Pro30 isomers of a novel 38-residue toxin from the venom of *Hadronyche infensa sp*. that contains a cystine-knot motif within its four disulfide bonds, *Biochemistry.* **41**, 3294–3301.
35. King GF, Middlehurst CR & Kuchel PW (1986) Direct NMR evidence that prolidase is specific for the *trans* isomer of imidodipeptide substrates, *Biochemistry.* **25**, 1054–1062.

36. Mobli M, Stern AS, Bermel W, King GF & Hoch JC (2010) A non-uniformly sampled 4D HCC(CO)NH-TOCSY experiment processed using maximum entropy for rapid protein sidechain assignment, *J Magn Reson.* **204**, 160–164.
37. Guntert P (2004) Automated NMR structure calculation with CYANA, *Methods Mol Biol.* **278**, 353–378.
38. Shen Y, Delaglio F, Cornilescu G & Bax A (2009) TALOS+: a hybrid method for predicting protein backbone torsion angles from NMR chemical shifts., *J Biomol NMR.* **44**, 213–223.
39. Pallaghy PK, Nielsen KJ, Craik DJ & Norton RS (1994) A common structural motif incorporating a cystine knot and a triple- stranded β-sheet in toxic and inhibitory polypeptides, *Protein Sci.* **3**, 1833–1839.
40. Kwan AH, Mobli M, Gooley PR, King GF & Mackay JP (2011) Macromolecular NMR spectroscopy for the non-spectroscopist, *FEBS J.* **278**, 687–703.
41. Davis IW, Leaver-Fay A, Chen VB, Block JN, Kapral GJ, Wang X, Murray LW, Arendall WB, 3rd, Snoeyink J, Richardson JS & Richardson DC (2007) MolProbity: all-atom contacts and structure validation for proteins and nucleic acids, *Nucl Acids Res.* **35**, 375–383.
42. Holm L & Rosenström P (2010) Dali server: conservation mapping in 3D, *Nucl Acids Res.* **38**, W545–W549.
43. Fujitani N, Kouno T, Nakahara T, Takaya K, Osaki T, Kawabata S-i, Mizuguchi M, Aizawa T, Demura M, Nishimura S-I & Kawano K (2007) The solution structure of horseshoe crab antimicrobial peptide tachystatin B with an inhibitory cystine-knot motif, *J Pept Sci.* **13**, 269–279.
44. Hui K, Lipkind G, Fozzard HA & French RJ (2002) Electrostatic and steric contributions to block of the skeletal muscle sodium channel by μ-conotoxin, *J Gen Physiol.* **119**, 45–54.
45. Shon KJ, Olivera BM, Watkins M, Jacobsen R, Gray WR, Floresca CZ, Cruz LJ, Hillyard DR, Brink A, Terlau H & Yoshikami D (1998) μ-Conotoxin PIIIA, a new peptide for discriminating among tetrodotoxin-sensitive Na channel subtypes, *J Neurosci.* **18**, 4473–4481.
46. Bosmans F & Swartz KJ (2010) Targeting voltage sensors in sodium channels with spider toxins, *Trends Pharmacol Sci.* **31**, 175–182.

47. Bosmans F, Rash L, Zhu S, Diochot S, Lazdunski M, Escoubas P & Tytgat J (2006) Four novel tarantula toxins as selective modulators of voltage-gated sodium channel subtypes, *Mol Pharmacol.* **69**, 419–429.

48. Li D, Xiao Y, Hu W, Xie J, Bosmans F, Tytgat J & Liang SP (2003) Function and solution structure of hainantoxin-I, a novel insect sodium channel inhibitor from the Chinese bird spider *Selenocosmia hainana*, *FEBS Lett.* **555**, 616–622.

49. Wang R-l, Yi S & Liang S-P (2010) Mechanism of action of two insect toxins huwentoxin-III and hainantoxin-VI on voltage-gated sodium channels., *J Zhejiang Univ Sci B.* **11**, 451–457.

50. Billen B, Vassilevski AA, Nikolsky A, Tytgat J & Grishin EV (2008) Two novel sodium channel inhibitors from *Heriaeus melloteei* spider venom differentially interacting with mammalian channel's isoforms, *Toxicon.* **52**, 309–317.

51. Gordon D, Karbat I, Ilan N, Cohen L, Kahn R, Gilles N, Dong K, Stühmer W, Tytgat J & Gurevitz M (2007) The differential preference of scorpion α-toxins for insect or mammalian sodium channels: implications for improved insect control, *Toxicon.* **49**, 452–472.

52. Gilles N, Harrison G, Karbat I, Gurevitz M, Nicholson GM & Gordon D (2002) Variations in receptor site-3 on rat brain and insect sodium channels highlighted by binding of a funnel-web spider δ-atracotoxin, *Eur J Biochem.* **269**, 1500–1510.

53. Strichartz G & Wang G (1986) Rapid voltage-dependent dissociation of scorpion α-toxins coupled to Na channel inactivation in amphibian myelinated nerves, *J Gen Physiol.* **88**, 413–435.

54. Schreibmayer W, Kazerani H & Tritthart HA (1987) A mechanistic interpretation of the action of toxin II from *Anemonia sulcata* on the cardiac sodium channel, *Biochim Biophys Acta.* **901**, 273–282.

55. Grolleau F, Stankiewicz M, Birinyi-Strachan L, Wang X, Nicholson GM, Pelhate M & Lapied B (2001) Electrophysiological analysis of the neurotoxic action of a funnel-web spider toxin, δ-atracotoxin-Hv1a, on insect voltage-gated Na^+ channels, *J Exp Biol.* **204**, 711–721.

56. Yamaji N, Little MJ, Nishio H, Billen B, Villegas E, Nishiuchi Y, Tytgat J, Nicholson GM & Corzo G (2009) Synthesis, solution structure, and phylum selectivity of a spider δ-toxin

that slows inactivation of specific voltage-gated sodium channel subtypes, *J Biol Chem.* **284**, 24568–24582.

57. Corzo G, Sabo JK, Bosmans F, Billen B, Villegas E, Tytgat J & Norton RS (2007) Solution structure and alanine scan of a spider toxin that affects the activation of mammalian voltage-gated sodium channels., *J Biol Chem.* **282**, 4643–4652.
58. Bosmans F, Rash L, Zhu S, Diochot S, Lazdunski M, Escoubas P & Tytgat J (2006) Four novel tarantula toxins as selective modulators of voltage-gated sodium channel subtypes, *Mol Pharmacol.* **69**, 419–429.
59. King GF, Gentz MC, Escoubas P & Nicholson GM (2008) A rational nomenclature for naming peptide toxins from spiders and other venomous animals, *Toxicon.* **52**, 264–276.
60. Little MJ, Zappia C, Gilles N, Connor M, Tyler MI, Martin-Eauclaire M-F, Gordon D & Nicholson GM (1998) δ-Atracotoxins from Australian funnel-web spiders compete with scorpion α-toxin binding but differentially modulate alkaloid toxin activation of voltage-gated sodium channels, *J Biol Chem.* **273**, 27076–27083.
61. Zlotkin E, Rochat H, Kopeyan, Miranda F & Lissitzky S (1971) Purification and properties of the insect toxin from the venom of the scorpion *Androctonus australis* Hector, *Biochimie.* **53**, 1073–1078.
62. Fletcher JI, Chapman BE, Mackay JP, Howden MEH & King GF (1997) The structure of versutoxin (δ-atracotoxin-Hv1) provides insights into the binding of site 3 neurotoxins to the voltage-gated sodium channel, *Structure.* **5**, 1525–1535.
63. Wang X-H, Connor M, Smith R, Maciejewski MW, Howden MEH, Nicholson GM, Christie MJ & King GF (2000) Discovery and characterization of a family of insecticidal neurotoxins with a rare vicinal disulfide bond., *Nat Struct Biol.* **7**, 505–513.
64. Mobli M, de Araujo AD, Lambert LK, Pierens GK, Windley MJ, Nicholson GM, Alewood PF & King GF (2009) Direct visualization of disulfide bonds through diselenide proxies using ^{77}Se NMR spectroscopy, *Angew Chem Int Ed.* **48**, 9312–9314.
65. Reily MD, Holub KE, Gray WR, Norris TM & Adams ME (1994) Structure-activity relationships for P-type calcium channel-selective omega-agatoxins, *Nat Struct Mol Biol.* **1**, 853–856.
66. Ferrat G, Bosmans F, Tytgat J, Pimentel C, Chagot B, Gilles N, Nakajima T, Darbon H & Corzo G (2005) Solution structure of two insect-specific spider toxins and their

pharmacological interaction with the insect voltage-gated Na^+ channel, *Proteins.* **59**, 368–379.

67. Omecinsky DO, Holub KE, Adams ME & Reily MD (1996) Three-dimensional structure analysis of μ-agatoxins: further evidence for common motifs among neurotoxins with diverse ion channel specificities, *Biochemistry.* **35**, 2836–2844.
68. Bogan AA & Thorn KS (1998) Anatomy of hot spots in protein interfaces., *J Mol Biol.* **280**, 1–9.
69. Smith JJ, Hill JM, Little MJ, Nicholson GM, King GF & Alewood PF (2011) Unique scorpion toxin with a putative ancestral fold provides insight into evolution of the inhibitor cystine knot motif, *Proc Natl Acad Sci USA.* **108**, 10478–10483.
70. Sunagar K, Undheim EA, Chan AH, Koludarov I, Munoz-Gómez SA, Antunes A & Fry BG (2013) Evolution stings: the origin and diversification of scorpion toxin peptide scaffolds, *Toxins.* **5**, 2456–2487.
71. Fang L, Jia K, Tang Y, Ma D, Yu M & Hua Z (2007) An improved strategy for high-level production of *TEV* protease in *Escherichia coli* and its purification and characterization, *Protein Expr Purif.* **51**, 102–109.
72. Hoch JC, Maciejewski MW, Mobli M, Schuyler AD & Stern AS (2014) Nonuniform sampling and maximum entropy reconstruction in m ultidimensional NMR, *Acc Chem Res.* **47**, 708–717.
73. Mobli M, Maciejewski MW, Gryk MR & Hoch JC (2007) An automated tool for maximum entropy reconstruction of biomolecular NMR spectra, *Nat Meth.* **4**, 467–468.
74. Fletcher JI, Smith R, O'Donoghue SI, Nilges M, Connor M, Howden MEH, Christie MJ & King GF (1997) The structure of a novel insecticidal neurotoxin, ω-atracotoxin-HV1, from the venom of an Australian funnel web spider, *Nat Struct Biol.* **4**, 559–566.
75. Barry PH (1994) JPCalc, a software package for calculating liquid junction potential corrections in patch-clamp, intracellular, epithelial and bilayer measurements and for correcting junction potential measurements, *J Neurosci Meth.* **51**, 107–116.

Tables

Table 1. Structural statistics for ensemble of 20 NMR structures of rSf1a[1].

Experimental restraints[2]	
Interproton distance restraints	
Intraresidue	147
Sequential	225
Medium range (i–j < 5)	58
Long range (i–j ≥ 5)	134
Disulfide-bond restraints	12
Dihedral-angle restraints (36 ϕ, 39 ψ)	75
Total number of restraints per residue	13.9
R.m.s. deviation from mean coordinate structure (Å)	
All backbone atoms (residues 1–45)	0.80 ± 0.18
All heavy atoms (residues 1–45)	1.24 ± 0.19
Backbone atoms (residues 4–26,39–45)	0.13 ± 0.03
Heavy atoms (residues 4–26,39–45)	0.43 ± 0.06
Stereochemical quality[3]	
Residues in most favored Ramachandran region (%)	82.4 ± 2.4
Ramachandran outliers (%)	0.4 ± 0.9
Unfavorable sidechain rotamers (%)	6.8 ± 3.1
Clashscore, all atoms[4]	0.0 ± 0.0
Overall MolProbity score	1.55 ± 0.18

[1]All statistics are given as mean ± S.D.

[2]Only structurally relevant restraints, as defined by CYANA, are included.

[3]According to MolProbity (http://molprobity.biochem.duke.edu).

[4]Defined as the number of steric overlaps >0.4 Å per thousand atoms.

Figure Legends

Figure 1: Production and functional analysis of rSf1a. **(A)** Schematic representation of the pLicC-NSB2 vector used for periplasmic expression of rSf1a. The coding region includes a MalE signal sequence ($MalE_{SS}$) for periplasmic export, a His_6 affinity tag, an MBP fusion tag, and a codon-optimized gene encoding rSf1a, with a TEV protease recognition site inserted between the MBP and toxin coding regions. The locations of key elements of the vector are shown, including the ribosome-binding site (RBS), T7 promoter and lac operator. (B) Primary structure of rSf1a. The non-native N-terminal Ser residue is highlighted in grey. Disulfide-bridge connectivities are indicated above the sequence. **(C)** SDS-PAGE gels illustrating different steps in purification of rSf1a. Lanes are as follows: M, molecular weight markers; lane 1, *E. coli* cell extract prior to IPTG induction; lane 2, *E. coli* cell extract after IPTG induction; lane 3, soluble periplasmic extract (the His_6-MBP-rSf1a fusion protein is evident at ~50 kDa); lane 4, Ni-NTA beads after loading the cell lysate; lane 5, eluate resulting from passage of cell lysate through Ni-NTA resin; lane 6, eluate from washing Ni-NTA resin with 10 mM imidazole; lane 7, eluate from washing Ni-NTA resin with 500 mM imidazole; lane 8, sample after TEV protease cleavage, showing complete cleavage of the MBP-Sf1a fusion protein. **(D)** RP-HPLC chromatogram showing the final step in the purification of rSf1a. The arrow denotes the peak corresponding to correctly folded recombinant rSf1a. Inset is a MALDI-TOF MS spectrum showing the $[M+H]^+$ ion for the purified recombinant toxin (obs. = 5058.25 Da; calc. = 5056.98 Da). **(E)** Paralytic effects of two versions of recombinant Sf1a following injection in sheep blowflies (*L. cuprina*). nat-Sf1a corresponds to the native sequence, while Ser-Sf1a is recombinant toxin with an additional non-native N-terminal serine residue. Paralysis was determined 24 h after injection.

Figure 2: Inhibition of cockroach DUM neuron Na_V channels by rSf1a. **(A and C)** Representative superimposed I_{Na} traces before (black), and following (grey and shaded), application of 1 μM (A) and 10 μM (C) rSf1a. Dotted lines represent zero current. **(Ba)** pulse protocol used to generate I_{Na} shown in panel A. (D) Incomplete inhibition of I_{Na} by increasing concentrations of rSf1a (grey bars) and 1 μM rSf1a-R31A-W33A (open bar). **(E)** Typical timecourse of I_{Na} inhibition by 1 μM rSf1a. Data were fitted with Eq. 3. **(F)** Effects of depolarizing post-pulses on dissociation of rSf1a were assessed using 10-ms post-pulses to +140 mV applied immediately following a test pulse to –10 mV from –90 mV as detailed in panel Bb. I_{Na} were normalized to peak control I_{Na} before (closed circles), and after (open circles), application of 1 μM rSf1a.

Figure 3: The effects of rSf1a on the voltage-dependence of Na_V gating in cockroach DUM neurons. **(A-B)** Voltage protocols used to generate I_{Na}. **(C-D)** Typical superimposed families of I_{Na} are shown before **(C),** and after **(D),** application of 1 μM rSf1a. Currents were generated using the test pulse protocol shown in panel A. **(E-F)** Normalized I_{Na}-V relationships before (closed circles), and after (open circles and shaded), application of 1 μM rSf1a generated using the pulse protocol in panel B. Data were fitted with Eq. 1 (see Materials and Methods). Currents were normalized against maximum peak I_{Na} in controls **(E)** and maximum peak I_{Na} **(F)**. **(G-H)** Effects of rSf1a on steady-state Na_V channel inactivation (h_∞) were determined using a two-pulse protocol detailed in panel B. Peak I_{Na} recorded during the test pulse before (closed circles), and after (open circles and shaded), application of 1 μM rSf1a were normalized to maximum inward I_{Na} in controls **(G)** and maximum inward I_{Na} **(H)** and plotted against pre-pulse potential. The h_∞-V curves were fitted with Eq. 2 (see Materials and Methods).

Figure 4: Effects of rSf1a on Ca_V and K_V channel currents in cockroach DUM neurons. **(A–D)** Inhibition of barium currents through cockroach DUM neuron Ca_V channels by rSf1a. **(A and B)** Representative superimposed I_{Ba} traces before (black), and following (grey and shaded), application of 1 μM rSf1a to M-LVA **(A)** and HVA **(B)** channels. Dotted lines represent zero current. Currents were generated using the test pulse protocol shown in panel Ca. **(D)** Normalized I_{Ba}-V relationships before (closed circles), and after (open circles and shaded), application of 1 μM rSf1a. Currents were generated using the test pulse protocol shown in panel Cb. Normalized I_{Ba}-V relationships were fitted using Eq. 2. **(E–H)** Inhibition of cockroach DUM neuron K_V channels by rSf1a. **(E)** Representative superimposed I_K traces before (black), and following (grey and shaded), application of 1 μM rSf1a. Dotted lines represent zero current. Currents were generated using the test pulse protocol shown in panel Fa. **(G and H)** Normalized global I_K-V relationships before (closed circles), and after (open circles and shaded), application of 1 μM rSf1a on peak **(G)** and late **(H)** I_K. Currents were generated using the test pulse protocol shown in panel Fb and measurements for peak and late current were measured at the circle and square (50 ms) shown in panel E, respectively. Normalized I_K-V relationships were fitted using Eq. 2.

Figure 5: 2D ^{1}H-^{15}N HSQC NMR spectrum of rSf1a acquired at 900 MHz. Sequence-specific resonance assignments are indicated. Backbone amide assignments are annotated using the one-letter amino acid code. Assignments are also shown for the sidechain NH correlations of Trp33, the sidechain NH_2 groups of the four Asn residues, and the aliased peak from the sidechain of Arg31. (Note: numbering according to the native sequence).

Figure 6: Three dimensional structure of rSf1a. **(A)** Ensemble of 20 NMR-derived structures. β-strands are green, while the disulfide bonds are shown as yellow sticks. The dominant extended and largely disordered loop is highlighted in red. (Note: numbering according to the native sequence). **(B)** The ensemble is rotated such that the ICK motif is clearly visible. The ICK ring formed by two disulfide bonds is shown in magenta and the third ICK disulfide bond piercing this ring is also shown. The remainder of the molecule is made transparent for clarity. **(C)** Overlay of rSf1a (red) with structural homologs tachystatin B (PDB 2DCV; blue) and Aps III (PDB 2M36; green). The structures are made transparent while the disulfide bonds are shown as solid sticks, illustrating the alignment of the ICK motif. The position of the extra disulfide bond that serves as a molecular staple in Sf1a and Aps III is also shown.

Figure 1

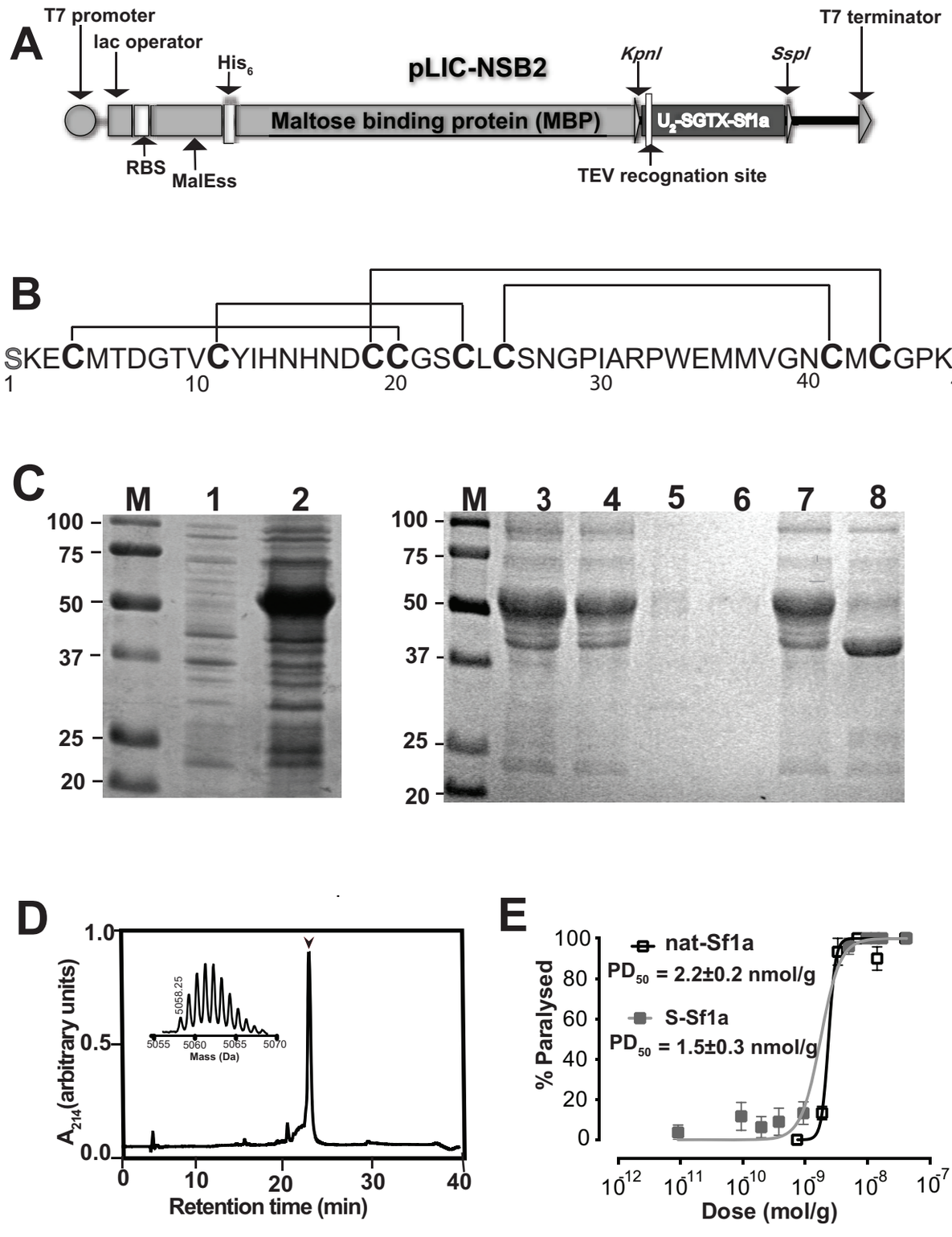
A
T7 promoter
lac operator
His6
pLIC-NSB2
KpnI
SspI
T7 terminator
Maltose binding protein (MBP)
U2-SGTX-Sf1a
RBS
MalEss
TEV recognation site
B
SKECMTDGTVCYIHNHNDCCGSCLCSNGPIARPWEMMVGNCMCGPKA
1
10
20
30
40
47
C
M
1
2
3
4
5
6
7
8
100
75
50
37
25
20
D
A214(arbitrary units)
1.0
0.5
0.0
5058.25
5055
5060
5065
5070
Mass (Da)
0
10
20
30
40
Retention time (min)
E
% Paralysed
nat-Sf1a
PD50 = 2.2±0.2 nmol/g
S-Sf1a
PD50 = 1.5±0.3 nmol/g
100
80
60
40
20
0
10-12
10-11
10-10
10-9
10-8
10-7
Dose (mol/g)

Figure 2

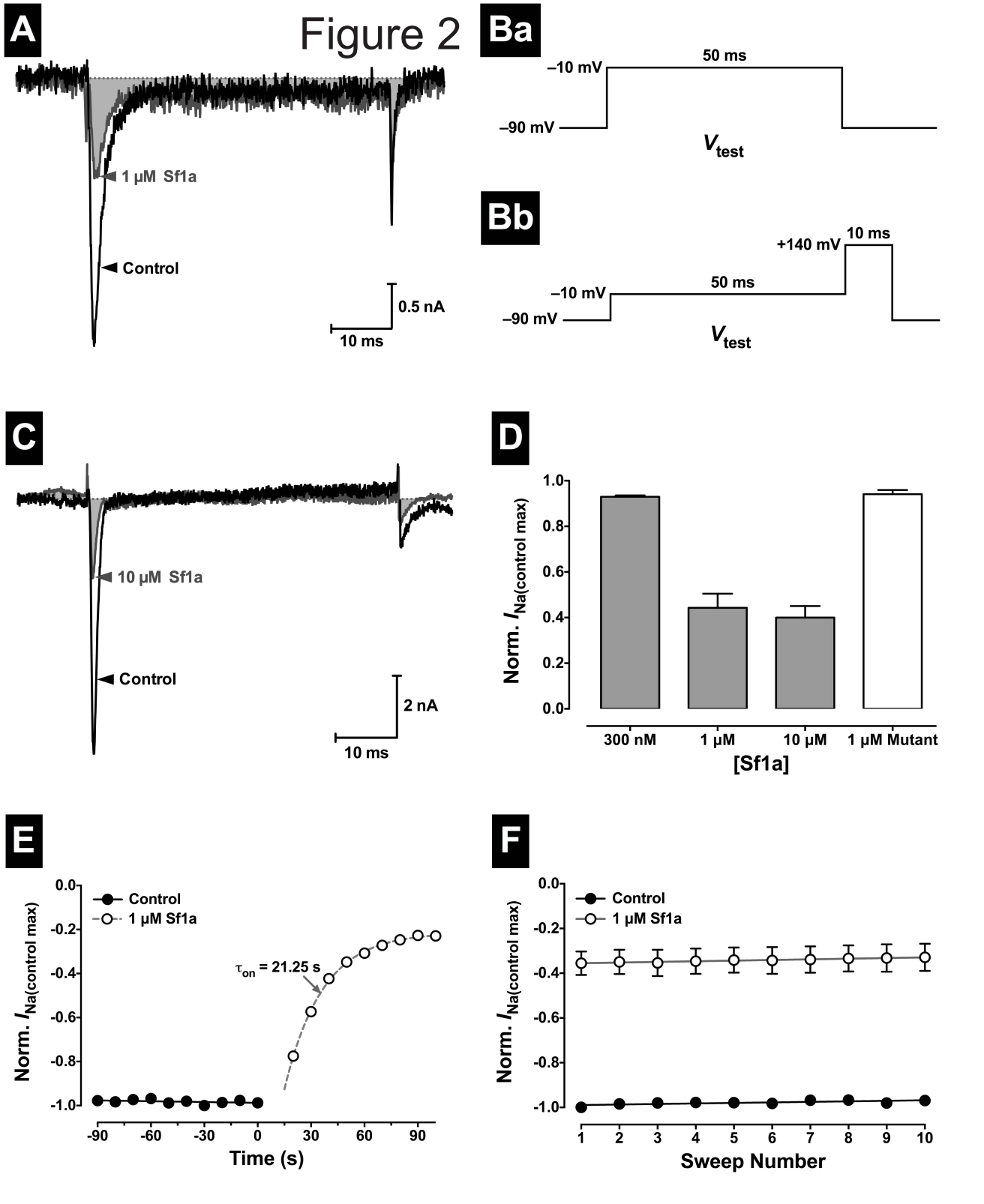
A
1 μM Sf1a
Control
0.5 nA
10 ms
Ba
50 ms
–10 mV
–90 mV
V_{test}
Bb
10 ms
+140 mV
50 ms
–10 mV
–90 mV
V_{test}
C
10 μM Sf1a
Control
2 nA
10 ms
D
Norm. $I_{Na(control\ max)}$
1.0
0.8
0.6
0.4
0.2
0.0
300 nM
1 μM
10 μM
1 μM Mutant
[Sf1a]
E
Control
1 μM Sf1a
τ_{on} = 21.25 s
Norm. $I_{Na(control\ max)}$
0.0
-0.2
-0.4
-0.6
-0.8
-1.0
-90
-60
-30
0
30
60
90
Time (s)
F
Control
1 μM Sf1a
Norm. $I_{Na(control\ max)}$
0.0
-0.2
-0.4
-0.6
-0.8
-1.0
1
2
3
4
5
6
7
8
9
10
Sweep Number

Figure 3

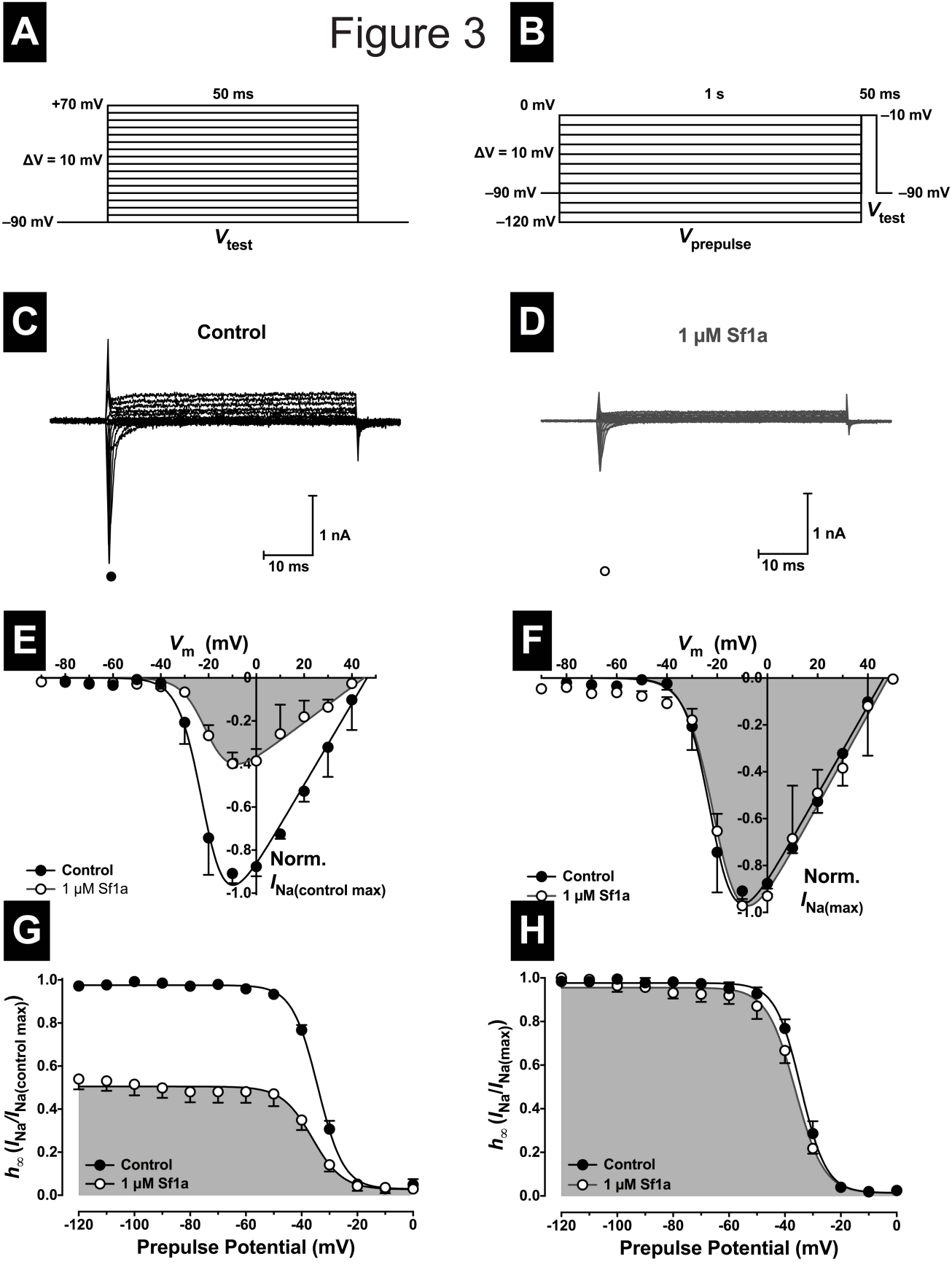
A
50 ms
+70 mV
ΔV = 10 mV
–90 mV
V_{test}
B
1 s
50 ms
0 mV
–10 mV
ΔV = 10 mV
–90 mV
–90 mV
–120 mV
V_{test}
$V_{prepulse}$
C
Control
1 nA
10 ms
D
1 µM Sf1a
1 nA
10 ms
E
V_m (mV)
-80 -60 -40 -20 0 20 40
0 -0.2 -0.4 -0.6 -0.8 -1.0
Norm. $I_{Na(control max)}$
Control
1 µM Sf1a
F
V_m (mV)
-80 -60 -40 -20 0 20 40
0.0 -0.2 -0.4 -0.6 -0.8 -1.0
Norm. $I_{Na(max)}$
Control
1 µM Sf1a
G
h_∞ ($I_{Na}/I_{Na(control max)}$)
1.0 0.8 0.6 0.4 0.2 0.0
Control
1 µM Sf1a
-120 -100 -80 -60 -40 -20 0
Prepulse Potential (mV)
H
h_∞ ($I_{Na}/I_{Na(max)}$)
1.0 0.8 0.6 0.4 0.2 0.0
Control
1 µM Sf1a
-120 -100 -80 -60 -40 -20 0
Prepulse Potential (mV)

Figure 4

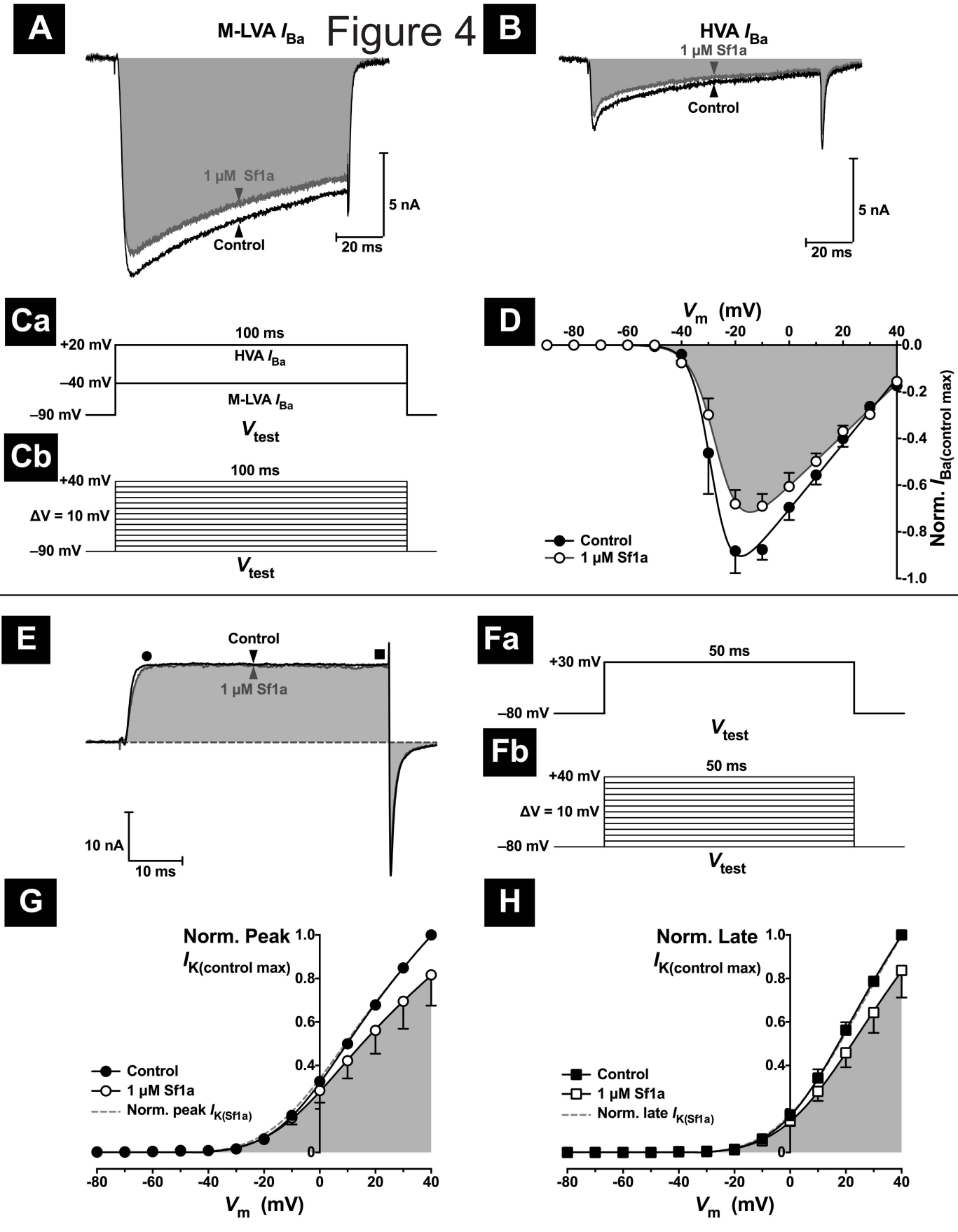
A
M-LVA I_{Ba}
1 μM Sf1a
Control
5 nA
20 ms
B
HVA I_{Ba}
1 μM Sf1a
Control
5 nA
20 ms
Ca
100 ms
+20 mV
HVA I_{Ba}
–40 mV
M-LVA I_{Ba}
–90 mV
V_{test}
Cb
100 ms
+40 mV
ΔV = 10 mV
–90 mV
V_{test}
D
V_m (mV)
-80 -60 -40 -20 0 20 40
0.0 -0.2 -0.4 -0.6 -0.8 -1.0
Norm. $I_{Ba(control max)}$
Control
1 μM Sf1a
E
Control
1 μM Sf1a
10 nA
10 ms
Fa
50 ms
+30 mV
–80 mV
V_{test}
Fb
50 ms
+40 mV
ΔV = 10 mV
–80 mV
V_{test}
G
Norm. Peak $I_{K(control max)}$
1.0 0.8 0.6 0.4 0
Control
1 μM Sf1a
Norm. peak $I_{K(Sf1a)}$
-80 -60 -40 -20 0 20 40
V_m (mV)
H
Norm. Late $I_{K(control max)}$
1.0 0.8 0.6 0.4 0
Control
1 μM Sf1a
Norm. late $I_{K(Sf1a)}$
-80 -60 -40 -20 0 20 40
V_m (mV)

Figure 5

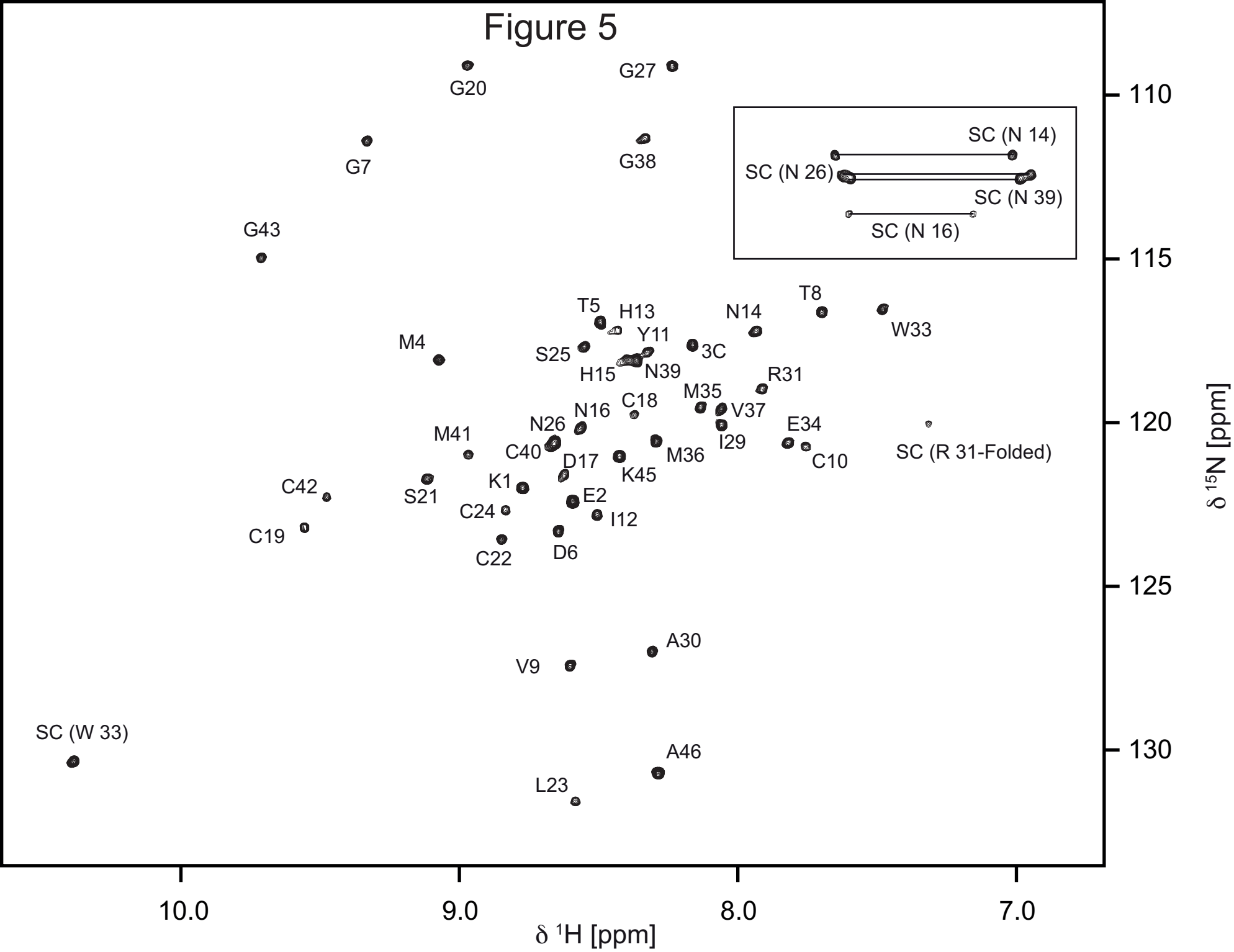
G20
G27
G7
G38
G43
SC (N 14)
SC (N 26)
SC (N 39)
SC (N 16)
T8
T5
H13
N14
W33
M4
Y11
S25
3C
H15
N39
R31
M35
C18
N16
V37
N26
E34
M41
I29
C40
D17
M36
C10
SC (R 31-Folded)
K45
C42
K1
S21
E2
C24
I12
C19
D6
C22
A30
V9
SC (W 33)
A46
L23
110
115
120
125
130
δ 15N [ppm]
10.0
9.0
8.0
7.0
δ 1H [ppm]

Figure 6

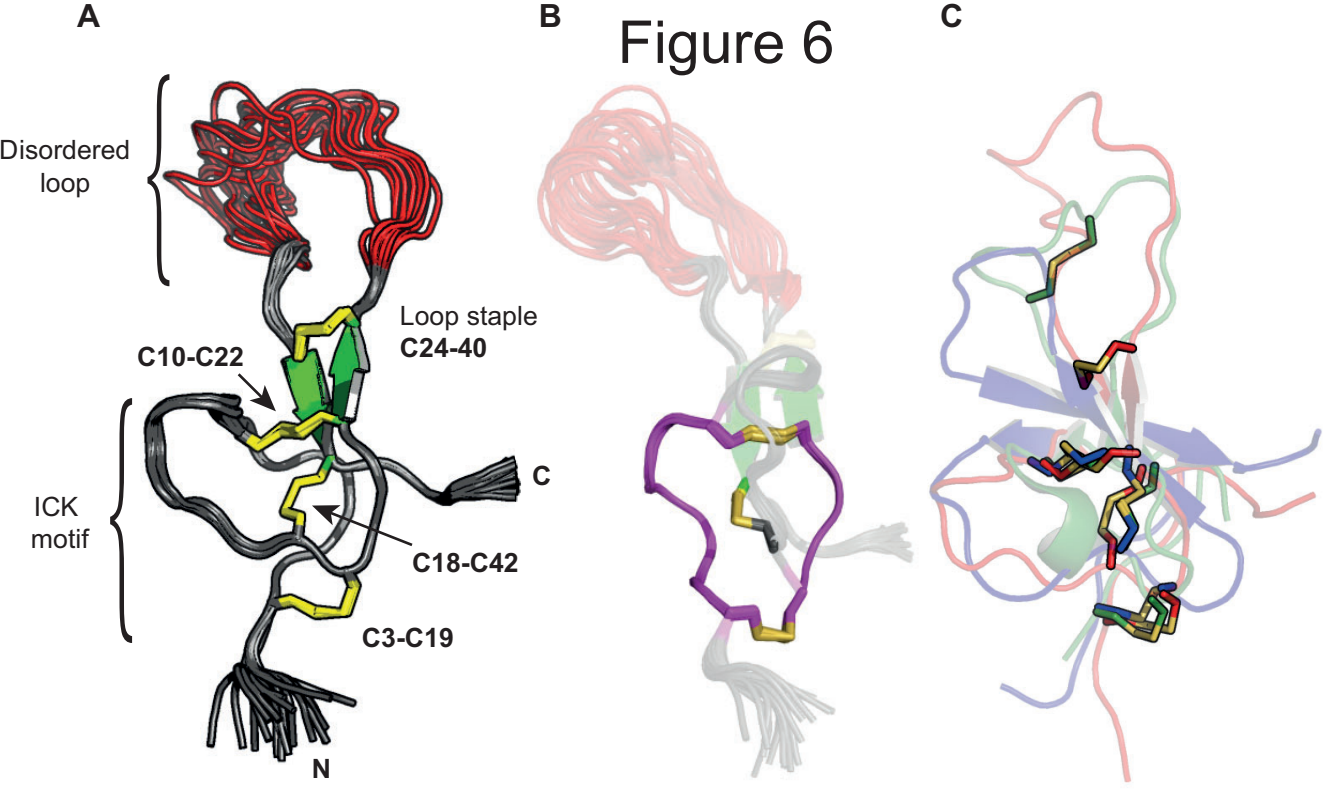
A
B
C
Disordered loop
Loop staple
C24-40
C10-C22
ICK motif
C
C18-C42
C3-C19
N